Available online at www.ijapie.org

International Journal of Advanced
Production and Industrial Engineering

IJAPIE-SI-IDCM 602 (2017) 04–11

Special Issue on

INNOVATIVE DESIGN
&
COMPUTATIONAL
MODELLING

Analysis on Drag Reduction of Bluff Body using Dimples

Shabir Grover[1,*], B.B.Arora[1], Vaibhav Khanna[1], Tushar Kaushik[1], Akhilesh Arora[1]
[1]*Department of Mechanical Engineering, Delhi Technological University, New Delhi-110042, India.*

Email: shabirgrover_2k14@dtu.ac.in

Abstract : *A comparative study based on numerical modelling of airflow over a smooth generic bluff body against a dimpled one has been taken up in the present study using a reformed CFD FLUENT code. The investigation of flow is carried out using an Ahmed body, 25 degrees rear slant with dimples incorporated on its top as well as rear slant surface with specifications, AR equal to 6.25, and diameter (Φ) 25mm. The turbulent characteristics of the air stream were examined using the reliable two equation k-ε model. For an enhanced study of adverse pressure gradients near surfaces, a non-equilibrium state was assumed for the wall interface. All in all, the simulation results show that a drag reduction of 0.3% was obtained by employing dimples with elliptical profile.*

Keywords: *Reynolds number, Turbulent flow, Flow separation, Drag Coefficient, Dimples, Form Drag*

I. INTRODUCTION

Nowadays, the rapid diminution of fossil fuels has posed a tremendous challenge for designers and engineers working in the automotive field to develop more fuel efficient vehicles. Implementing modifications to the exterior form of the vehicles has become paramount to decrease the drag force acting on them thereby, minimizing fuel consumption and maximizing efficiency.
Moreover, the ever increasing worries about ecological concerns over the past two decades, as well as the recent emergence of the energy crisis have accelerated this endeavour of drag reduction.

It has been established that for a medium sized European car, the aerodynamic drag force accounts for nearly 80% of the total road resistance at a 100 km/hr cruise speed. [16]

$$F_D = C_D \times A \times \frac{\rho}{2} \times V^2$$ [19]

Where C_D is the non-dimensional drag coefficient; A is the projected frontal area of the vehicle and ρ is the density of the surrounding air and $F_D$is the Drag force acting on the body.

Drag reduction attained through controlling air flow effects over a surface seems to be an answer to the above problems. Experimentally, this procedure of drag reduction and the development of the methods to control it were first carried out. But due to the higher costs involved in fabrication of wind tunnels and the inaccuracies achieved in similarity matching, experimental methods are proving to be unfeasible. Nowadays, the analysis of an engineering system relies heavily on computer-based solution algorithms which utilize numerical techniques to obtain approximate solutions for the governing partial differential equations (PDE). Computational fluid dynamics (CFD) has emerged as one such essential tool, which is more than widely employed in the automotive industry. Due to the massive advances in computational power, the time and costs required to carry out simulations have reduced significantly.

There has been several work carried out in the past for drag reduction using both active and passive flow control devices. Although, active flow devices have shown greater improvement in efficiency and performance during all phases of operation, but passive flow control devices have proved themselves to be more desirable due to their greater reliability, short profile and no external energy requirement. Active flow control, on the other hand, involves addition of energy or momentum to the system in a regulated manner and has shown a tendency to increase the complexity and weight of the system drastically.

One such passive method is the use of dimples as a means for increasing surface roughness to reduce drag. Previous work has shown that the total drag force experienced by a generic bluff body is a combination of pressure drag and skin friction drag in which the former predominates the latter. The application of dimples on golf balls has shown that dimpled golf balls have a lower coefficient of drag, C_D than non-dimpled ones, which is due to the delaying of the flow separation at the rear end. Thus, the dimpled golf balls are able to travel relatively longer distances. This favourable reduction in drag is caused by the dimples on its surface which “trip” the boundary layer to transition from laminar to turbulent flow, whose mechanism is similar to vortex generators. This happens because turbulent flow stays attached for a longer period due to the greater component of momentum in the direction of flow and this delays flow separation. This delay in flow separation decreases form

drag, which in turn leads to a decrease in the total drag force acting on it. Total drag force is composed of form drag and drag due to skin friction.

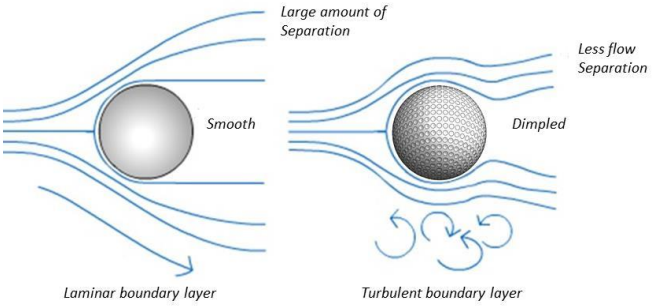

Fig. 1 Effect of dimples on golf ball

While there is an increase in surface roughness due to the presence of dimples, the skin friction component of total drag gets scaled up. Since the golf ball is a bluff body, the component of form drag is more dominant as compared to drag due to skin friction. Overall, the combined effect of dimples on the surface of the golf ball translates in to a reduced total drag coefficient.

$$C_D^{Total} = C_D^{Form} + C_D^{Skin\ Friction}$$

Where $C_D^{Skin\ Friction}$ and C_D^{Form} are the non-dimensional coefficients of skin friction drag and pressure/form drag respectively. Their algebraic sum along with taking into account interference drag, gives the coefficient of parasitic drag or in this case total drag coefficient i.e. C_D^{Total}.

In spite of this work, the underlying mechanisms through which the dimpled surfaces affect the transition of the boundary layer from laminar to turbulent have not been fully explored to the extent that accurate prediction of aerodynamic forces of lift and drag and their corresponding moments is possible. The present work is intended to assess the flow regime, total coefficient of drag value and to ascertain the fact that the result obtained lies in close proximity with the experimentally determined value.

II. Literature Survey

The study undertaken is a mere consequence of the present day situation of road cars and the fuel availability. Extensive development in the automotive arena has led to increased average cruising speeds for road cars. This consequently has brought the problem of aerodynamic drag to the forefront which was earlier considered imperceptible. It thus turns out that significant drag force experienced by cars has led to investigation into the techniques using which the coefficient of drag value for vehicles can be reduced.

A thorough study of previously published research papers has revealed that vehicle parameters alone do not affect total drag; operational parameters have a large effect as well. Here, only passive methods have been researched.

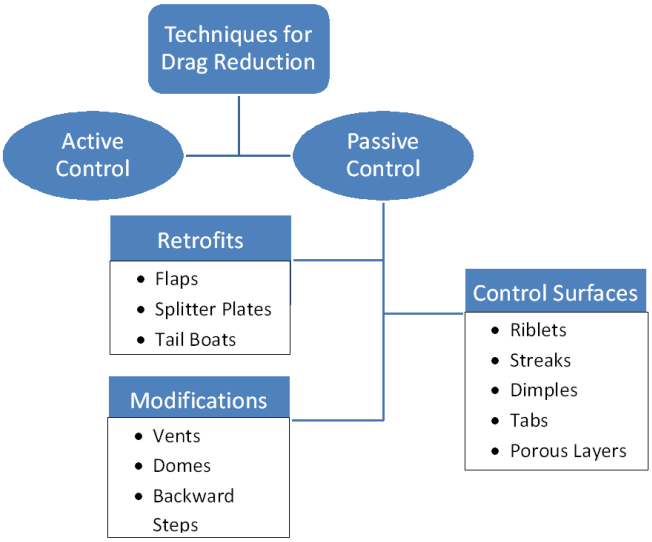

Fig. 2 Methods for drag reduction

A. *Retrofits*

A. Fillippone and Muhammed-Kassim (2008) conducted a numerical study on various drag reducing retrofits with the aim of saving fuel. It was found that using aerodynamics devices is beneficial only when the vehicles travel at high speeds as weight does not have any direct effect on drag. In other cases such as city driving condition their usage is not justifiable. Commonly used retrofits are splitter plate, boat tails, flaps or deflectors.

B. *Control Surfaces*

Katsumi Aoki et al (2012) tried to clarify the mechanism of drag reduction for a sphere with arc type dimples. Pressure and velocity distributions were measured inside and between the dimples and the flow over the sphere was visualised by an oil filling method.

C. *Modifying and Optimizing Existing Designs*

Hsu and Davis (2008) found that by adding humps on the top, bottom and/or sides of trailer along with boat-tail flaps can reduce drag by about 50.9%. But the method isn't viable for real automobiles.

All the above examples are a testimony to the fact that reasonably good amount of investigation has been carried out in this field but still the hypothesis of turbulent boundary layer remaining attached to the body surface for long has not found a sound explanation. Thus extensive research work is still being carried out.

III. METHODOLOGY

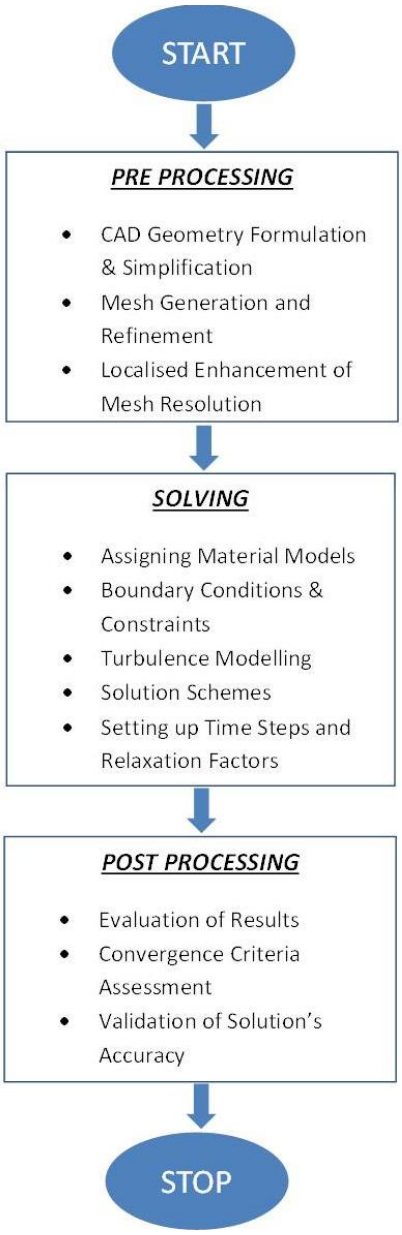

Fig. 3 Framework of CFD

A. *Vehicle Body*

In the present study, a typical bluff body called as the Ahmed body with 25 degrees rear slant angle was utilized. The Ahmed body is a simplified car model which is used for studying the flow simulation carried over the body. But it still retains the prominent features of a car namely, a curved fore body, a straight centre section and the angled rear end. The 3 dimensional CAD model of the body was drafted by using DS Solidworks using the dimensional details available from the research carried out by S.R. Ahmed. After the default model is drafted, it will be added with the formulated profile of dimple at the top surface or roof. For the placement of the dimples on the top surface, a linear patterned configuration was put in to use.

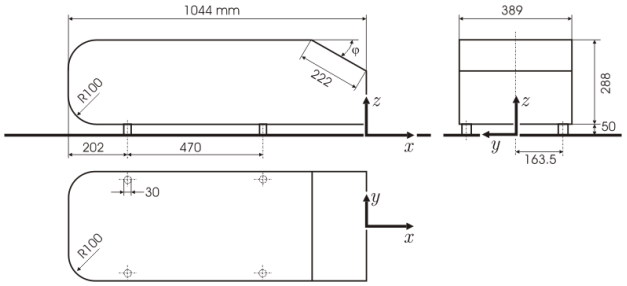

Fig. 4 Dimensions of Ahmed body, given slant angle φ = 25 degrees

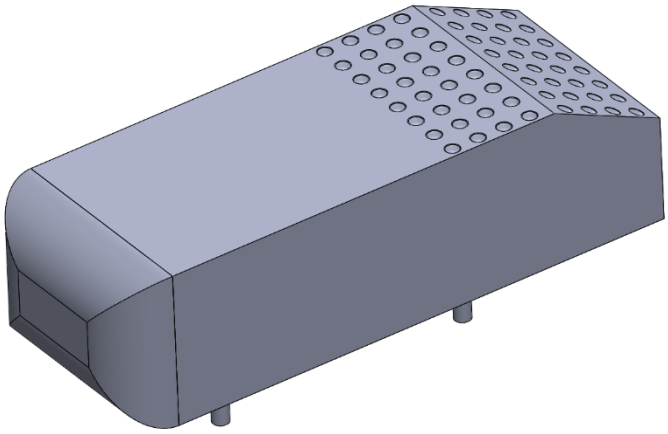

Fig. 5 Trimetric view of dimpled Ahmed body

B. *Aspect Ratio*

In order to completely define the dimple specifications, the parameter Aspect Ratio (AR) has been introduced. This quantity is the ratio of the diameter of the dimple to its depth i.e. (D/h).This implies that for a given dimple Diameter (Φ) and its AR, the dimple depth can be determined.

Significant differences in dimple geometry – due to variations in diameter, aspect ratio, fillet radius, relative positioning of dimples and the profile implicitly determine by how much the Coefficient of Drag will be affected.

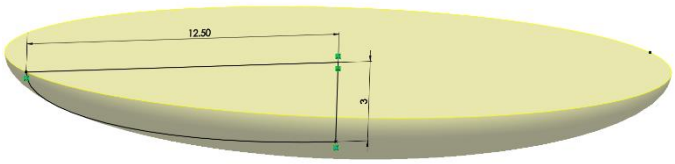

Fig. 6 Dimple geometry incorporated on the Ahmed body

C. *Meshing*

The meshing is done by using ICEM CFD ANSYS meshing software. The computational domain exists between 13.544m X 6.389m X 3.338m. Blockage area ratio of 0.539% is used, which is significantly lesser than the maximum limit of 7.5%. In order to decrease the total computational time, a symmetry plane passing through the Ahmed Body's longitudinal axis is created. This effectively reduces the number of elements and nodes by half. A hybrid mesh topology was adopted –

comprising of both structured and unstructured grids. For regions of inviscid flow, such as the region pertaining to the outside of the boundary layer where local shear stresses are negligible, tetrahedral elements are more dominant. In the regions of viscid flow, like the boundary layers around Ahmed Body's surface, prismatic elements are utilized in order to effectively resolve the velocity profiles for the analysis. For a typical car-like shape, pressure drag is dominant over skin friction, so the accuracy of the drag predictions are largely determined by the accuracy of the predicted static pressure distribution on the body. This pressure distribution is strongly affected by the locations of flow separation and reattachment.

Therefore it is important that the surface mesh resolves all relevant details of the geometry and satisfies the requirements of the physical models used in the simulation.

Prismatic elements provide good alignment with the flow near wall boundaries. This is beneficial for reducing numerical diffusion. Thus, flat regions, especially on the front part of the under-body as well as the top surface containing dimples should be resolved using prismatic layers. The transition between the two types of elements was also kept gradual so as to prevent the distortion of the elements, while also merging the nodes at the interfaces. This not only kept the number of elements low, but at the same time increased the accuracy of the results.

TABLE I
SETUP DETAILS FOR MESH AND SOLVING SCHEME

Particulars	Type of Body	
	Uncontrolled	Controlled
Element Type	Tetra/Prismatic (Flat Base)	Tetra/Prismatic (Flat Base)
Elements	4137591	5787095
Nodes	818485	1288770
Skewness (Maximum)	0.8959	0.8618
Orthogonal Quality (Minimum)	0.2009	0.227
Scheme Deployed	COUPLED	SIMPLE →COUPLED
Cores Utilized (Processors)	4	4
Computational Time	9 Hours	15 Hours
Processing Type	Parallel (Single Precision)	Parallel (Single Precision)

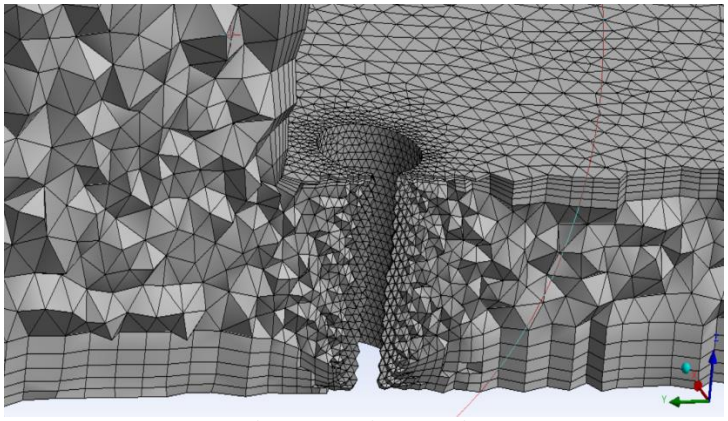

Fig. 7 Cut section view of enhanced refinement of mesh near dimples

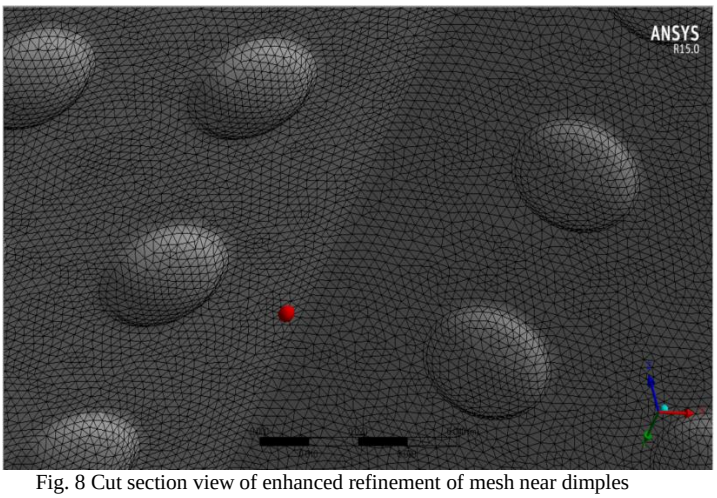

Fig. 8 Cut section view of enhanced refinement of mesh near dimples

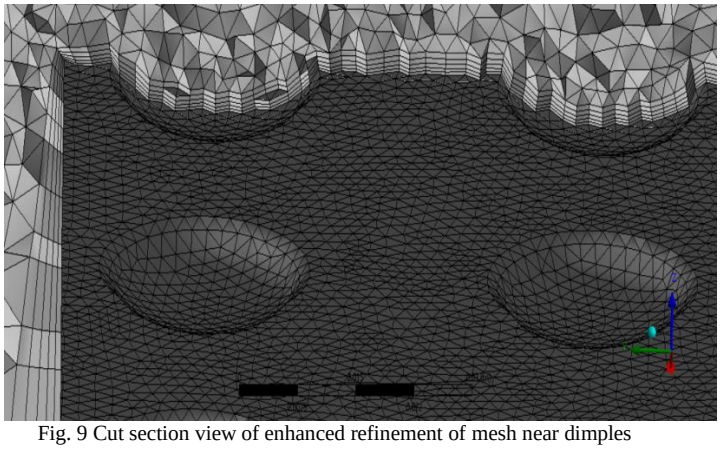

Fig. 9 Cut section view of enhanced refinement of mesh near dimples

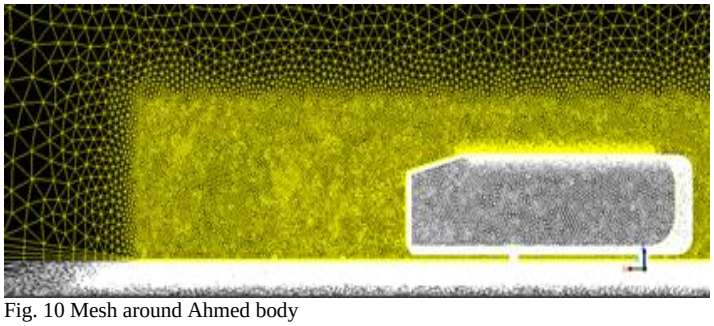

Fig. 10 Mesh around Ahmed body

D. *Turbulence Model*

In this paper, the turbulence model chosen was a realizable *k-ϵ* model with non-equilibrium wall functions. This was done due to its robustness and high degree of versatility, which tends to produce accurate solutions. Also the computational time required for performing Large Eddy Simulation (LES) was proving to be infeasible as compared to Reynolds Averaged Navier-Stokes (RANS) model. Similarly, Direct Numerical Simulation (DNS) would've required a grid with an enormously high level of mesh resolution. All of the above reasons led to the selection of RANS equations with the *k-ϵ* turbulence model. It comprises of two transport equations to represent the turbulent properties of the flow. The first transport variable is the kinetic energy term, *k*. It is the variable to determine the turbulent energy production.

$$\frac{\partial}{\partial t}(\rho k) + \frac{\partial}{\partial x_i}(\rho k u_j) = \frac{\partial}{\partial x_i}\left[\left(\mu + \frac{\mu_t}{\sigma_k}\right).\frac{\partial k}{\partial x_j}\right] + G_k + G_b - \rho\epsilon - Y_M + S_k$$

The second transport variable is the turbulent dissipation term, ϵ. It is the variable to determine the scales of the turbulence.

$$\frac{\partial}{\partial t}(\rho\epsilon) + \frac{\partial}{\partial x_j}(\rho\epsilon u_j) = \frac{\partial}{\partial x_j}\left[\left(\mu + \frac{\mu_t}{\sigma_\epsilon}\right).\frac{\partial \epsilon}{\partial x_j}\right] + \rho C_1 S_\epsilon - \rho C_2 \frac{\varepsilon^2}{k+\sqrt{\upsilon\epsilon}} + C_{1\epsilon}\frac{\epsilon}{k}C_{3\epsilon}G_b + S_\epsilon$$

In the equations above, G_k is the generation of turbulence kinetic energy due to the mean velocity gradients. G_b is the generation of turbulence kinetic energy due to buoyancy. Y_m is the contribution of the fluctuating dilatation in compressible turbulence to the overall dissipation rate. $C_{1\epsilon}$ and C_2
σ_k and σ_ϵ re constants and turbulent Prandtl numbers for *k* and ϵ respectively. S_k and S_ϵ are user defined source terms.

E. *Governing Equations* [20]

1) *Continuity Equation:*

$$\frac{\partial \rho}{\partial t} + \nabla.(\rho V) = 0$$

2) *Conservation of Momentum in x –direction:*

$$\frac{\partial(\rho u)}{\partial t} + \frac{\partial(\rho u^2)}{\partial x} + \frac{\partial(\rho uv)}{\partial y} + \frac{\partial(\rho uw)}{\partial z} =$$

3)

$$-\frac{\partial p}{\partial x} + \frac{\partial\left(\lambda\nabla.V + 2\mu\frac{\partial u}{\partial x}\right)}{\partial x} + \frac{\partial\left(\mu\left[\frac{\partial v}{\partial x} + \frac{\partial u}{\partial y}\right]\right)}{\partial y} + \frac{\partial\left(\mu\left[\frac{\partial u}{\partial z} + \frac{\partial w}{\partial x}\right]\right)}{\partial z} + \rho f_x$$

4) *Conservation of Momentum in y –direction:*

$$\frac{\partial(\rho v)}{\partial t} + \frac{\partial(\rho uv)}{\partial x} + \frac{\partial(\rho v^2)}{\partial y} + \frac{\partial(\rho vw)}{\partial z} =$$

$$-\frac{\partial p}{\partial y} + \frac{\partial\left(\mu\left[\frac{\partial v}{\partial x} + \frac{\partial u}{\partial y}\right]\right)}{\partial x} + \frac{\partial\left(\lambda\nabla.V + 2\mu\frac{\partial v}{\partial y}\right)}{\partial y} + \frac{\partial\left(\mu\left[\frac{\partial w}{\partial y} + \frac{\partial v}{\partial z}\right]\right)}{\partial z} + \rho f_y$$

5) *Conservation of Momentum in z –direction:*

$$\frac{\partial(\rho w)}{\partial t} + \frac{\partial(\rho uw)}{\partial x} + \frac{\partial(\rho vw)}{\partial z} + \frac{\partial(\rho w^2)}{\partial y} =$$

$$-\frac{\partial p}{\partial z} + \frac{\partial\left(\mu\left[\frac{\partial u}{\partial z} + \frac{\partial w}{\partial x}\right]\right)}{\partial x} + \frac{\partial\left(\mu\left[\frac{\partial w}{\partial y} + \frac{\partial v}{\partial z}\right]\right)}{\partial y} + \frac{\partial\left(\lambda\nabla.V + 2\mu\frac{\partial w}{\partial z}\right)}{\partial z} + \rho f_z$$

F. *Boundary Conditions*

In this work, the free stream velocity has been set to 40 m/s at the inlet (with a turbulence intensity of 1%), related to the overall length of the model that gives the Reynolds number as;

$$R_e = \frac{\rho UL}{\mu} = \frac{1.225 \times 40 \times 1.044}{1.789 \times 10^{-5}} = 2.86\times 10^6$$

Where ρ is the density of air; is the flow velocity; *L* is the characteristic length of the car model; μ is the coefficient of dynamic viscosity of air.

The pressure outlet is maintained at a gauge pressure of 0 Bar with 5% turbulence intensity at the exit.

In case of the mid-plane which is parallel to the longitudinal axis of the Ahmed Body and passes through the geometric centre, it was kept as a symmetry plane, which eased up the calculation time required for the simulation.

No slip conditions as applicable on the surfaces of the body, along with zero shear stresses acting on the walls of the fluid domain or the control volume were taken into consideration.

Reference values were computed from the velocity inlet with respect to the global/absolute co-ordinate system.

IV. Setup

Parallel processing was employed for finding out the solution up to single precision. A total of four threads were run simultaneously to carry out the simulations.

Upon defining the conditions in the setup instead of Density based, Pressure Based Navier Stokes (PBNS) was utilised (gravitational effects neglected). Originally, PBNS was used for working with incompressible flows, also since the maximum velocity in the flow-field will be less than Mach number 0.3, relative density changes will be less than 5 per cent. Another reason is that the convergence in density based heavily depends upon several factors since density is derived from the equation of continuity, whereas the state equation is used to obtain the values of pressure.

The solution scheme employed is the coupled scheme for the entire iterations of the uncontrolled (non-dimpled) case while for the controlled case the solution was initially solved using the simple scheme (first order upwind) so as to ensure a decreasing trend for continuity. Later after about 1200 iterations the solving scheme was shifted to the coupled scheme (second order upwind), which takes second order approximations for solving the turbulent kinetic energy and dissipation terms i.e. k and ϵ for ultimately solving the drag value.

Hybrid initialisation was used. The convergence criteria were kept up to e^{-5}. This gives considerably accurate solutions.

Also oscillation of continuity provided an indicator that the result was converged.

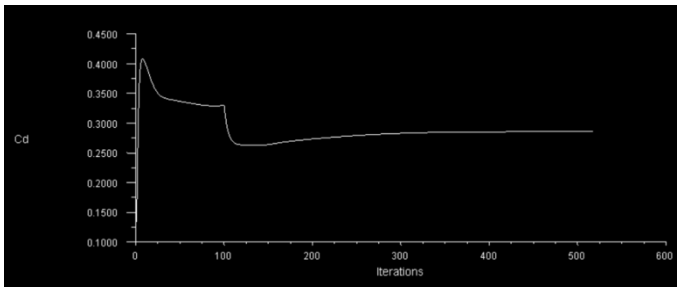

Fig. 11 Cd convergence history for the non-dimpled Ahmed body

V. Results

A. Static Pressure Contour

Figures 11 and 12 depict the distribution of static pressure over the grooved surfaces. The static pressure at velocity inlet and the pressure outlet of the domain is taken to be 0 Bar (gauge pressure). Although its distribution over the surface is rather uniform for almost the entire surface expect a few regions which are of specific interest. As the flow passes over the leading edge of the slant face it accelerates thereby reducing the static pressure value all along the edge. Also, along the direction of flow the periphery of the dimples reflect a greenish ting showing that the pressure value has mellowed down at those points. This phenomenon is observed due to acceleration in the flow both upstream as well as downstream of the dimple as it encounters the depression, thus creating a low pressure region just around the periphery of the dimple. This pressure differential is higher in the longitudinal direction of flow. Another fact worth mentioning is that the intensity of the low pressure increases as we move towards the outer end/edge of the body. This is due to the stream-wise counter rotating vortices which are formed because of the low pressure prevailing on the slant surface compared to side face. The axis of the vortices so formed is along the direction of the slant.

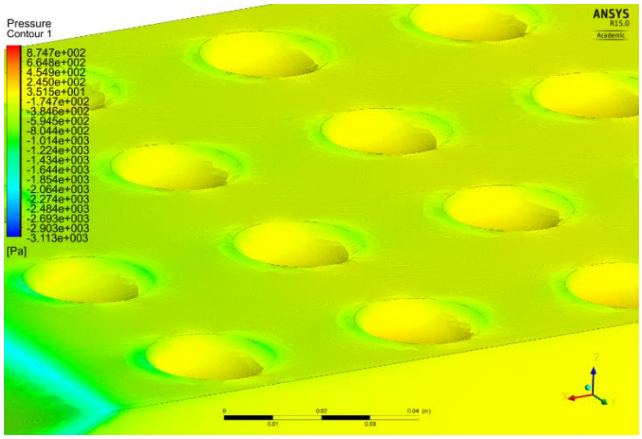

Fig. 12 A surface plot showing the static pressure variation on the top surface and the leading edge of the slant surface

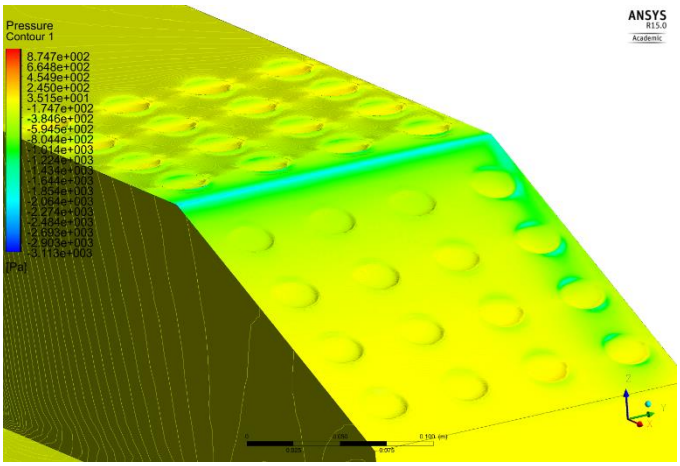

Fig. 13 Low pressure zone created towards the outer edge of the slant surface due to the edge rotating vortices

B. Velocity Volume Rendering

Figure 13 gives a 3-D partially transparent velocity distribution to describe the flow characteristics over the body. As can be seen, there exist 2 major regions of low velocity zone (less than 40m/s) i.e. the one just before the front face or upstream of the body and the other just downstream of the body. The former zone is due to the stagnation of flow at the front face with the highest intensity at the centre point as the flow collides with the body head on. As we move away from the epicentre the intensity subsides as the flow starts gliding over the curved faces though in a constrained manner. The latter low velocity zone is formed due to flow separation taking place and the flow reversals incurred as the flow no longer remains attached to the surface. However, the flow lines ultimately meet further downstream and thus a gradual increase in intensity can be seen. The flow accelerating over the curved faces and over the leading slant edge as well as

remaining attached to the top and bottom faces due to no slip condition are some of the key features visible.

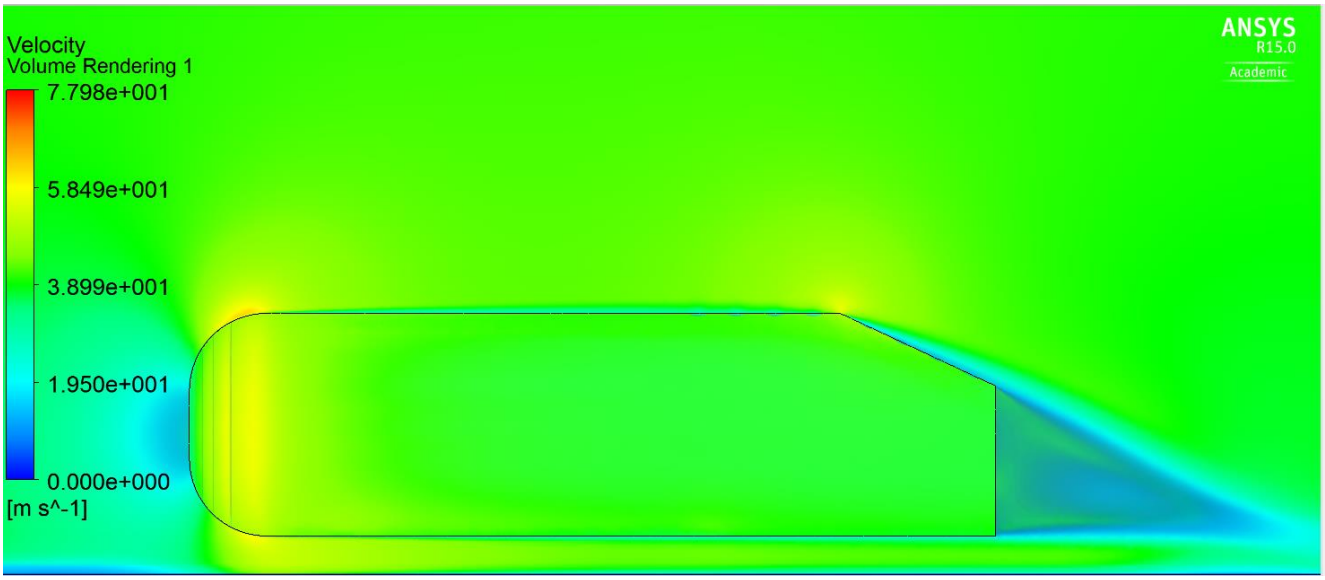

Fig. 14 Velocity volume rendering for the grooved body showing low velocity zones including the most prominent wake region

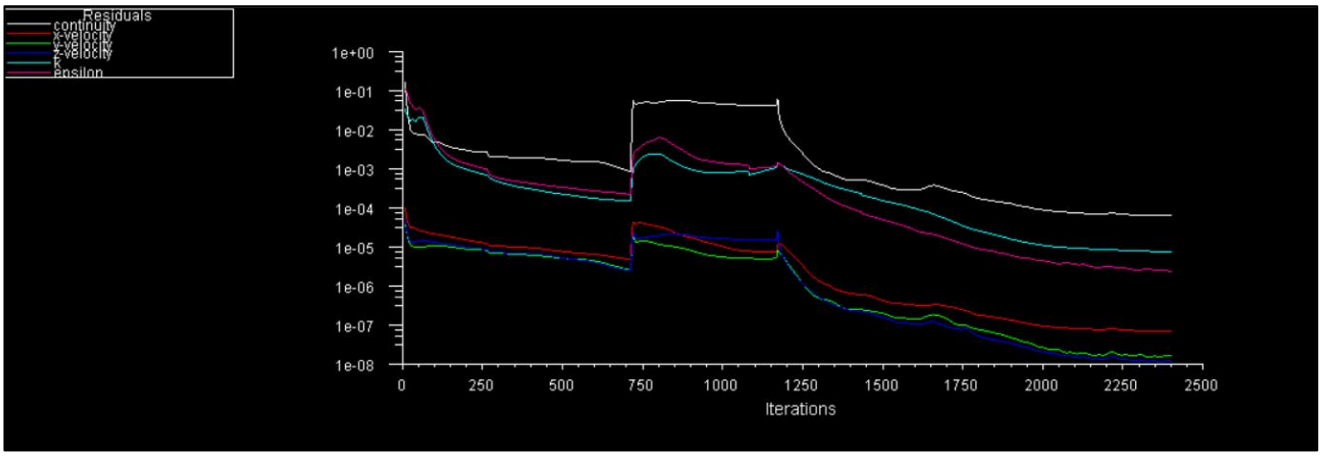


```
2389  6.6163e-05  7.2066e-08  1.7207e-08  1.2605e-08  7.6109e-06  2.5090e-06  3.6794e-01  2.8781e-01 -1.7449e+02  0.0000e+00  7.5426e+
2390  6.5770e-05  7.2126e-08  1.7186e-08  1.2551e-08  7.5965e-06  2.4926e-06  3.6794e-01  2.8781e-01 -1.7449e+02  0.0000e+00  7.5425e+
2391  6.5584e-05  7.1883e-08  1.7177e-08  1.2469e-08  7.5998e-06  2.4718e-06  3.6794e-01  2.8781e-01 -1.7449e+02  0.0000e+00  7.5425e+
2392  6.5258e-05  7.1981e-08  1.7181e-08  1.2429e-08  7.5855e-06  2.4594e-06  3.6794e-01  2.8781e-01 -1.7449e+02  0.0000e+00  7.5424e+
2393  6.5278e-05  7.1748e-08  1.7210e-08  1.2389e-08  7.5884e-06  2.4410e-06  3.6794e-01  2.8781e-01 -1.7449e+02  0.0000e+00  7.5425e+
2394  6.5281e-05  7.1762e-08  1.7264e-08  1.2321e-08  7.5733e-06  2.4233e-06  3.6794e-01  2.8781e-01 -1.7449e+02  0.0000e+00  7.5425e+
2395  6.5678e-05  7.1649e-08  1.7338e-08  1.2306e-08  7.5774e-06  2.4073e-06  3.6794e-01  2.8781e-01 -1.7449e+02  0.0000e+00  7.5425e+
2396  6.5035e-05  7.1640e-08  1.7311e-08  1.2265e-08  7.5612e-06  2.3887e-06  3.6794e-01  2.8781e-01 -1.7449e+02  0.0000e+00  7.5426e+
iter  continuity  x-velocity  y-velocity  z-velocity           k     epsilon        Cl-1        Cd-1  surf-mon-1  surf-mon-2  surf-mor
2397  6.4760e-05  7.1555e-08  1.7146e-08  1.2267e-08  7.5656e-06  2.3719e-06  3.6794e-01  2.8781e-01 -1.7449e+02  0.0000e+00  7.5426e+
2398  6.5111e-05  7.1681e-08  1.6978e-08  1.2219e-08  7.5500e-06  2.3541e-06  3.6794e-01  2.8781e-01 -1.7449e+02  0.0000e+00  7.5426e+
2399  6.5118e-05  7.1532e-08  1.6821e-08  1.2210e-08  7.5551e-06  2.3434e-06  3.6793e-01  2.8781e-01 -1.7449e+02  0.0000e+00  7.5426e+
iting "| gzip -2cf > C:\Users\Shabir Grover\Desktop\5th sem\minor project\Good simulations\donald trump\donald trump_files\dp0\FFF\Flu
iting temporary file C:\Users\SHABIR~1\AppData\Local\Temp\flntgz-41968 ...
ne.

2400  6.4859e-05  7.1669e-08  1.6681e-08  1.2172e-08  7.5398e-06  2.3310e-06  3.6793e-01  2.8781e-01 -1.7449e+02  0.0000e+00  7.5425e+
```

Fig. 15 Convergence history graph for the controlled case - abruptness due to change in solving scheme procedure.

VI. Conclusions

The velocity renderings and the pressure variations observed are in synchronisation with the experimental results. The dimple parameters were chosen based on the theoretical study of the flow around the body and the past results which led to a 0.3 % reduction in drag value. But there exists even greater scope for optimisation of the dimple geometry and its positioning over the body surfaces which can lead to a massive reduction in the drag coefficient.

Acknowledgment

The success of the completion of this project is strongly attributed to Dr. B.B. Arora under whose guidance the project has been taken. His knowledge on the subject and the constant motivation provided did go a long way which shaped the outcome in a beautiful manner. Also not to

forget the constant support provided by the parents, by the lab assistant, by our class peers and the blessings of the Almighty.

REFERENCES

[1] Hsu, F.-H., Davis, R. L., Drag reduction of tractor-trailers using optimized add-on devices, Journal. Fluids Engineering, 132(8), 084504. doi:10.1115/1.4001587

[2] C. K. Chear, S. S. Dol, Vehicle Aerodynamics: Drag Reduction by Surface Dimples, International Journal of Mechanical, Aerospace, Industrial, Mechatronic and Manufacturing Engineering Vol: 9, No: 1, 2015.

[3] S. F. Wong, S. S. Dol, Simulation study on vehicle drag reduction, International Journal of Mechanical, Aerospace, Industrial, Mechatronic and Manufacturing Engineering Vol:10, No:3, 2016

[4] Katsumi Aoki, Koji Muto, Hiroo Okanaga, Mechanism of Drag Reduction by Dimple Structures on a Sphere, Journal of Fluid Science and Technology Vol. 7, No. 1, 2012.

[5] Seong-Ho Seo, Chung-Do Nam, Cheol-Hyun Hong, Drag Reduction of a Bluff Body by Grooves Laid Out by Design of Experiment, Journal of Fluids Engineering, Nov. 2013, Vol. 135 / 111202-1.

[6] Laurent Dumas, Optimization and Computational Fluid Dynamics, pp 191-215, Springer Berlin Heidelberg Germany, 2008.

[7] Alaman Altaf, Ashraf A. Omar and Waqar Asrar, Review of Passive Drag Reduction Tecniques for Bluff Road Vehicles, IIUM Engineering Journal, Vol. 15, No. 1, 2014.

[8] Marco Lanfrit, Best practice guidelines for handling Automotive External Aerodynamics with FLUENT, Fluent Deutschland GmbH Germany.

[9] Mohamed-Kassim and Filippone, A. "Fuel savings on a heavy vehicle via aerodynamic drag reduction", Transportation Research Part D Vol.15. pp 275-285. (2010).

[10] Chainani. A and Perera. N, CFD Investigation of Airflow on a Model Radio Control Race Car, WCE 2008 Vol II, July 2 - 4, 2008, London, U.K.

[11] Yeung, W. W. H. and Parkinson, G. V., Analysis and Modeling of Pressure Recovery for Separated Reattaching Flows, ASME Journal of Fluids Engineering, Vol. 126, No. 3, pp. 355–361, 2004.

[12] Manoj Kumar, Arora, B. B. and Subhashis Maji, "Analysis of flow separation in wide angle annular diffusers," International Journal of Applied Engineering Research, Vol.5, No.20. (2010) pp. 3419-3428, ISSN 0973-4562

[13] B. B. Arora, Manoj Kumar and Subhashis Maji, "Study of Inlet conditions on Diffuser Performance," International Journal of Theoretical and applied Mechanics, Vol.5, No.2. (2010) pp. 201-221, ISSN 09736085.

[14] Noor, M. M., Wandel, Andrew P. and Yusaf, Talal, "Detail guide for CFD on the simulation of Biogas combustion in bluff body mild burner," International Conference on Mechanical Engineering Research (ICMER2013), 1-3 July 2013

[15] Yiping Wang, Cheng Wu, Gangfeng Tan and Yadong Deng, "Reduction in the aerodynamic drag around a generic vehicle by using a non-smooth surface", Journal of Automobile Engineering.

[16] Wolf-Heinrich Hucho, "Aerodynamics of Road Vehicles", SAE International, 1998.

[17] Joseph Katz, "Race Car Aerodynamics: Designing for Speed", 1995.

[18] Ahmed, S.R., Ramm, R., Faltin, G. : Some salient features of the time averaged ground vehicle wake, SAE Paper 840300 (1984)

[19] Yunus A. Çengel, John M. Cimbala, "Fluid Mechanics: Fundamentals and Applications", 2006.

[20] John D. Anderson, Jr. "Computational Fluid Dynamics: The Basics with Applocations", 1995